

# Jet interaction at supersonic cross flow conditions

F. Seiler<sup>1</sup>, P. Gnemmi<sup>1</sup>, H. Ende<sup>1</sup>, M. Schwenzer<sup>2</sup>, R. Meuer<sup>2</sup>

<sup>1</sup> French-German Research Institute of Saint-Louis (ISL), 5 Rue du Général Cassagnou, 68301 Saint-Louis Cedex, France

<sup>2</sup> TZN Forschungs- und Entwicklungszentrum Unterlüss GmbH, now Rheinmetall DETEC AG, Neuensothrietherstr. 20, 29343 Unterlüss, Germany

Received 7 May 2002 / Accepted 12 March 2003

Published online 16 May 2003 – © Springer-Verlag 2003

**Abstract.** The thrust produced by lateral jet systems has been successfully used for several years to control the flight trajectory, i.e., the maneuverability of spacecraft in the high atmosphere and in orbit. Recently this technology has also been applied to projectiles and rockets flying in the low atmosphere from sea level up to more than 10 km. At ISL, investigations have been performed with a 90 mm caliber full-scale projectile in order to study a special side jet controlling system at flight speeds of about 1500 m/s, i.e., Mach number  $M \approx 4.4$  at altitudes of 1.5 and 7.5 km. The High Energy ISL Shock Tunnel facility is used as a ground testing facility in which the flow around the projectile is studied at fully duplicated flight conditions. In the test facility the projectile is fixed inside the test chamber and the atmospheric air is set in motion flowing around the projectile test model. The air flow is generated in the ISL Shock Tunnel STB which is equipped for this purpose with a divergent square nozzle with an exit side length of 184 mm. A lateral gas jet is produced by combustng a solid propellant in a combustion chamber, placed inside the projectile. The powder gases are blown out laterally via a nozzle, creating a complex flow field by the interaction of the lateral jet with the external cross flow. Differential interferometry is used to visualize the behavior of the external flow field distorted by the lateral jet outflow. Numerical simulations have been performed based on steady state computations using the conservation equations of mass, momentum and energy. This was done to theoretically predict the development of the flow field around the projectile under the influence of the side jet. As final result the lateral force acting on the projectile is given as force and moment amplification factors,  $K_F$  and  $K_M$  respectively.

**Key words:** Shock tunnel, Flow modeling, Atmospheric flight conditions, Side jet control

## Nomenclature

$C_D$	Drag coefficient without incidence	$M_j$	Mach number of the jet flow
$C_p$	Pressure coefficient	$P$	Static pressure
$c_\mu$	Turbulence model constant	$Pfs$	Cross-flow static pressure
$D$	Projectile caliber	$Pr_t$	Turbulent Prandtl number
$F_i$	Interaction force	$q_j$	Heat fluxes
$F_j$	Jet thrust without the projectile external flow	$R_{Pt}$	Total pressures ratio
$h$	Static enthalpy	$S_{ui}, S_E$	Source terms
$H$	Total enthalpy	$T$	Static temperature
$K_F$	Force amplification factor	$Tfs$	Cross-flow static temperature
$K_M$	Moment amplification factor	$t$	Time
$k$	Turbulent kinetic energy	$u_i$	Fluid velocity in the $x_i$ -coordinate direction
$Mf$	Mach number of the external flow	$x_i$	Cartesian coordinates
$M_i$	Interaction moment	$\delta_{ij}$	Kronecker symbol ( $\delta_{ij} = 1$ if $i = j$ , $\delta_{ij} = 0$ if $i \neq j$ )
		$\varepsilon$	Dissipation of turbulent kinetic energy
		$\Gamma$	Molecular diffusivity
		$\lambda$	Thermal conductivity
		$\mu$	Dynamic viscosity
		$\mu_t$	Eddy viscosity
		$\rho$	Fluid density
		$\tau_{ij}$	Viscous stress tensor

Correspondence to: F. Seiler (e-mail: seiler@isl.tm.fr)

An abridged version of this paper was presented at the 23rd Int. Symposium on Shock Waves at Fort Worth, Texas, from July 22 to 27, 2001

## 1 Introduction

Flight control by means of lateral jets has been used since the beginning of space flight to navigate spacecraft in orbit or in the high atmosphere at high supersonic flow speeds. Recently, the speed of projectiles flying in the lower atmosphere has progressed to hypersonic speeds of Mach 6 or more. Usual tools for projectile flight control at subsonic and slight supersonic Mach numbers, i.e., moving wings or flaps, cannot be properly used in this hypersonic flow domain because of the fast response time needed, and the high pressures and heat fluxes present at the front part of these elements. Instead, lateral jet control technology applied to high speed combat projectiles for successfully hitting the target seems to be very encouraging. Investigations in this field have already been done worldwide.

At ISL, activities concerning the interference of lateral jets and hypersonic cross flow started in 1985 with a bibliographical report (Naumann and Srulijes 1985) followed by experimental investigations carried out with ISL's High Energy Shock Tube facilities (Seiler et al. 2001). In these studies a flat wing was equipped with one or more divert thrusters to analyze the efficiency of the interaction between laterally blowing gaseous cold or hot jets and the hypersonic cross flow. The aim of these tests was to investigate the thruster efficiency, i.e., on the possibility that the thruster force being increased by the interference between the jet and the cross-flow. The flat plate test series have been continued since 1999 with cylindrical projectiles equipped with side jet producing thrusters. Some of these investigations on a high-speed projectile designed by TZN (presently Rheinmetall DETEC) were reported by Gnemmi and Seiler (2000). For guidance and control, a special thruster engine was developed for side jet production by burning a solid propellant. Gnemmi and Seiler (2000) mainly discussed the theoretical part of the work whereas in the present study further details are presented about the experiment.

## 2 Demands on jet interaction modeling

A complex flow field develops by the interaction of the laterally blowing gas jet with the supersonic cross flow around a cylindrical body. The resulting jet plume is deflected and acts as a massive obstacle located on the surface of the projectile. Thus, as shown in Fig. 1, a strong bow shock is formed in the supersonic flow in front of the jet obstacle. Also a separation zone develops upstream of the jet (Zukoski and Spaide 1964). In this separation zone, the pressure acting on the body surface becomes higher than the static pressure in the outer air flow whereas it expands in the recirculation formed downstream of the side jet.

The test flow must contain all the features present in full-scale flight in order to accurately model the complex interacting flow around the projectile. In the interaction region are separation and recirculation zones, combined with mixing phenomena, which cannot be simulated using similarity laws where the projectile geometry is sim-

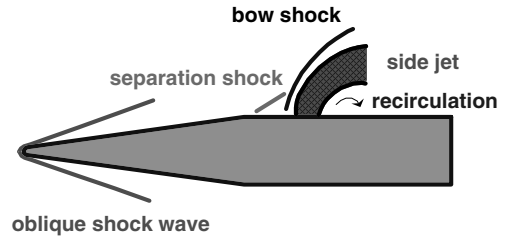


Fig. 1. Side jet interaction with supersonic cross flow

plified or the flow conditions deviate from that of actual flight. Furthermore, real gas effects have to be taken into account because the flow over the nose tip and in the separated region are influenced by nonequilibrium effects. For these reasons it is necessary to correctly model the flow to actual flight conditions. To achieve this requirement, the temperature, density, pressure, and flow velocity have to be duplicated with a full-scale projectile. Then, the total enthalpy equals the one reached at atmospheric flight conditions and the real stagnation temperature will be achieved. Air is used as test gas in order to model as realistically as possible the flight of the projectile under investigation in earth atmosphere.

With the side jet on, the jet's gases are blowing out of the thruster, followed by an interference with the air flow around the projectile. As a consequence, the thrust force is influenced by the interaction of cross and jet flow, thus disturbing the pressure distribution over the projectile surface. The total lateral side force exerted on the projectile by a divert thruster is made up by the thruster force  $F_j$  plus interference force  $F_i$ . The question to be answered in this study is whether the interference force  $F_i$  can be in the same direction as the thruster force giving a thrust amplification or on the opposite direction thus decreasing the efficiency of the side jet control system.

## 3 Shock tube as ground test facility

### 3.1 ISL's shock tunnel STB

There are two high pressure shock tubes, STA and STB, in the ISL Shock Tube Laboratory. Each of the two shock tubes, having 100 mm inner diameter, consists of a driver tube, a driven tube and a nozzle attached at the end of the driven tube. A diaphragm separates the driver tube containing helium and the driven tube containing air as the test gas. The driver gas is pressurized up to 60 MPa and the initial test gas fill pressure ranges from 100 kPa to 600 kPa, depending on the altitude conditions. After the diaphragm bursts, the shock wave that is formed inside the driven tube moves toward the end of the shock tube. At the nozzle throat, the incident shock wave is reflected, generating a quiescent high pressure and high temperature gas volume in front of the entrance to the nozzle. For these experiments the flow is accelerated inside a square divert nozzle with sides of 184 mm at the exit. The nozzle was designed for a flow Mach number of 4.5, but the actual test Mach number is about 4.4 for the experiments reported

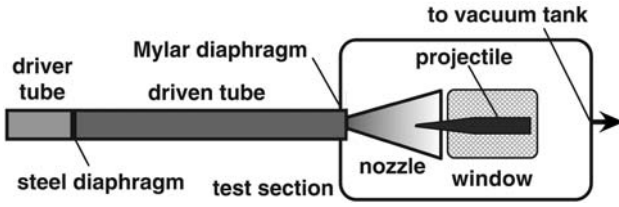


Fig. 2. Schematic assembly of shock tunnel STB

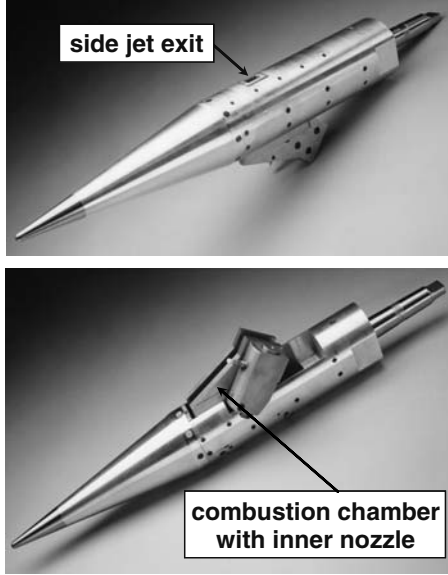


Fig. 3. Test model of TZN projectile

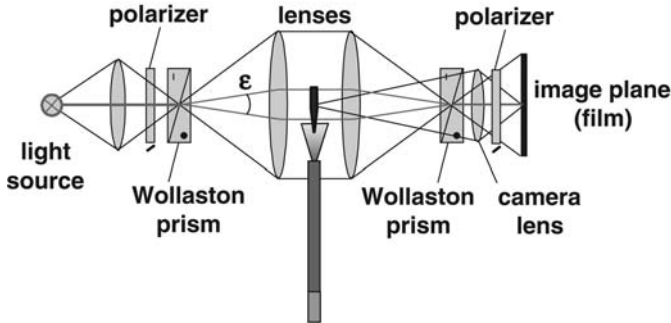


Fig. 4. Schematic of differential interferometer for visualizing the density gradient field

here. Figure 2 shows the schematic assembly of the shock tunnel STB.

The test conditions can be varied in the shock tube facility in order to fully duplicate flight conditions at altitudes from sea level up to more than 50 km. Test times of about 3 ms are obtained when the facility is operated as a reflected shock tunnel with tailored interface conditions. The experiments were performed at flight altitudes of 1.5 and 7.5 km. The corresponding static pressures are 85 and 38 kPa, while the corresponding static temperatures are 278 and 239 K. The flow conditions present at the nozzle exit were calculated and experimentally verified for the

two cases under investigation. The projectile is fixed on a special mounting system inside the test chamber in front of the nozzle exit.

### 3.2 Design of projectile model

The jet flow behavior on a jet-controlled cylindrical projectile model was studied at ISL in cooperation with TZN. TZN specially designed a hypervelocity projectile concept with regard to a 90 mm caliber. The total length of the projectile model is 6.45 calibers. The conical front portion is 3.25 calibers long, followed by the cylindrical body of 90 mm diameter, as shown in Fig. 3.

The half angle of the conical forebody is  $8.3^\circ$ . By combustion of a solid powder charge placed inside a combustion chamber the jet's gases are generated and are expanded via a specially designed nozzle into the external cross flow. The following averaged exit conditions are available as given by TZN calculations: static pressure  $p = 61$  kPa, temperature  $T = 1470$  K, flow speed  $u = 1700$  m/s,  $M = 2.2$ . In the experiments, the jet flow axis is directed perpendicular to the projectile surface (denoted as  $0^\circ$ ) or it is inclined by  $30^\circ$  in forward direction ( $-30^\circ$ ). The exit section is rectangular having an axial length of 21.5 mm for  $0^\circ$  jet axis angle, or 25 mm for  $-30^\circ$ , and 12.7 mm in transversal direction for both arrangements.

### 3.3 Flow visualization experiments

Windows at both sides of the test chamber allowed flow visualization. A differential interferometer (DI) that images density gradient fields is used (see Oertel sen. and Oertel jr. 1989) to gather information about the flow pattern around the projectile. Two perpendicularly polarized, expanded light beams are separated by a Wollaston prism (angle  $\epsilon$  in Fig. 4) and pass through the flow field in parallel, as shown in Fig. 4. The light beams are separated horizontally by some tenths of a millimeter from each other. The two expanded light beams are brought together by a second Wollaston prism, analyzed by a polarizer and are focused on a drum camera by a lens system. Density changes produced in the flow field generate different optical path lengths between the two split light beams, giving an interference pattern on the film inside the drum camera.

The DI can be adjusted to obtain fringe patterns or an infinite fringe width showing a homogeneous light intensity distribution. The infinite fringe adjustment method was used in the experiments. The infinite fringe differential interferograms look like schlieren pictures, showing changes of the density gradients in terms of light intensity variations.

A sequence of eight pictures was available on the drum camera for each shock tunnel test firing with an inter-frame time interval of  $400 \mu\text{s}$ . An air spark light source was used for illumination, giving eight successive spark

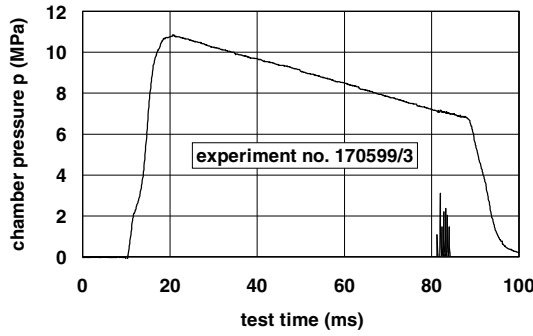


Fig. 5. Combustion chamber pressure (1.5 km altitude test)

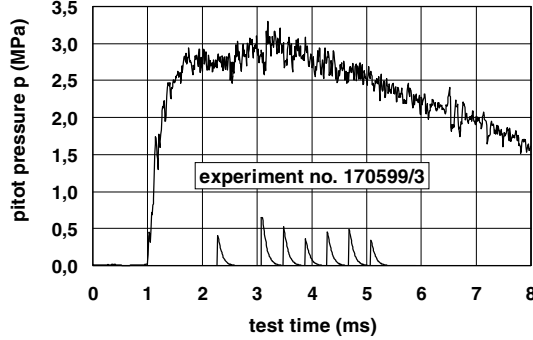


Fig. 6. Pitot chamber pressure (1.5 km altitude test)

peaks. The system is parallax free, i.e., the air sparks are formed always at the same local position.

Flow pictures are taken for three pitch angles,  $-4^\circ$  (tip down),  $0^\circ$ ,  $+4^\circ$  (tip up) and two orientations of the jet axis, perpendicularly to the projectile surface ( $0^\circ$ ) and a forward turn angle of  $-30^\circ$  against the jet axis. The ignition of the jet producing propellant is electrically triggered simultaneously with the shock tunnel firing.

A representative plot of the pressure distribution inside the combustion chamber is shown in Fig. 5 while the measured Pitot pressure for the same test firing for 1.5 km altitude conditions, is given in Fig. 6. In both Figs. 5 and 6, the illumination by the spark series is marked on the abscissa by the recorded diode light intensity peaks. As can be seen in Fig. 6, the second of the eight sparks for this experiment did not trigger.

An example of the eight differential interferograms is shown in Fig. 7 at  $0^\circ$  pitch angle and  $-30^\circ$  jet axis angle, for 1.5 km altitude conditions. The jet formation downstream along the surface of the projectile body is clearly visible by light intensity variations, showing variations in the density gradients arising from cross flow/jet interference. The shock wave in front of the side jet and the separation region upstream of the jet exit are well established. A white marker is placed in the photographs of Fig. 7 to indicate where the jet exits from the projectile surface.

From the picture sequence in Fig. 7, it can be seen that for about 3 ms a steady state jet/cross flow pattern develops, which clearly represents a short time section of the realistic flight scenario of a few seconds in the Earth's atmosphere. Nevertheless, the 3 ms test time allows the

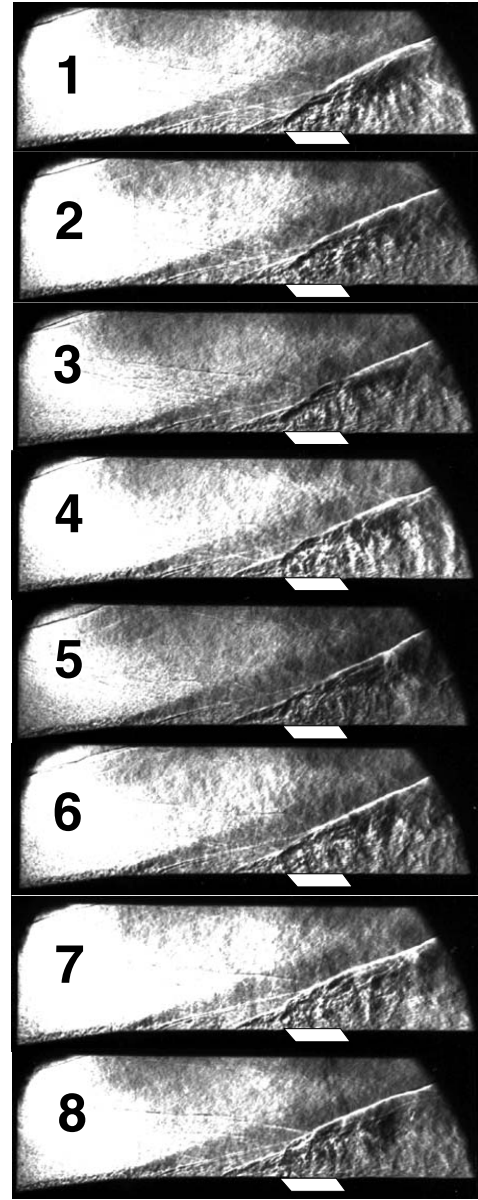
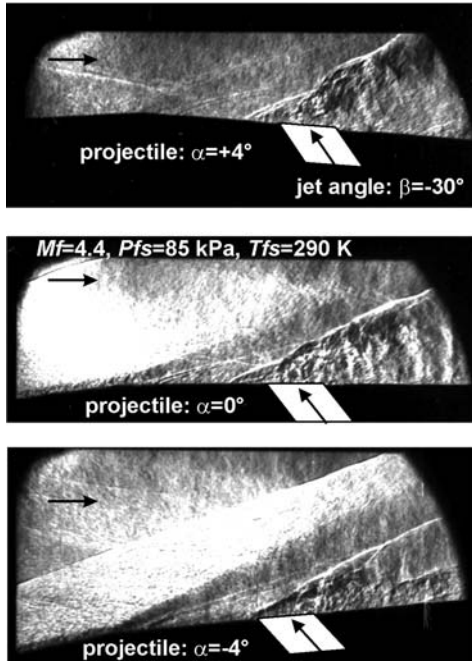


Fig. 7. Interferogram sequence with model at  $0^\circ$  pitch and  $30^\circ$  jet inclination

flow to fully develop so that all relevant data can be obtained. Using image 4 as a representative image, it can be seen that the region of influence of the downstream inclined jet extends over a large portion of the projectile surface, showing a strong interference between both, cross flow and jet.

Figure 8 depicts three interferograms of the projectile with a  $-30^\circ$  upstream inclined jet at projectile incidences of  $+4^\circ$ ,  $0^\circ$  and  $-4^\circ$ . The overpressure zone located upstream of the jet seems to be larger for the incidence of  $+4^\circ$ . This zone seems to be lowest for the incidence of  $-4^\circ$ . The position of the shock wave in front of the  $-30^\circ$  oriented jet obstacle is determined from the images. The shock angles, compared to the projectile surface, were measured as  $22^\circ$ ,  $26^\circ$  and  $30^\circ$  for  $-4^\circ$ ,  $0^\circ$  and  $+4^\circ$  pitch



**Fig. 8.** Interferogram pictures with  $-30^\circ$  jet angle, 1.5 km conditions

to an accuracy of  $\pm 1^\circ$ . The shock angle, compared to the direction of the parallel nozzle flow, is independent of the  $+4^\circ$ ,  $0^\circ$  and  $-4^\circ$  projectile pitch. The bow shock angle, relative to the nozzle flow direction, is  $26^\circ$ , as obviously visible in Fig. 8.

The angle between the jet-produced bow shock and the projectile surface with the jet axis oriented at  $0^\circ$  was determined as  $28^\circ$ ,  $32^\circ$  and  $36^\circ$  for  $-4^\circ$ ,  $0^\circ$  and  $+4^\circ$  pitch, with an accuracy of  $\pm 1^\circ$ . The jet obstacle increases with an increase of pitch. Again, the angle of the shock in front of the jet, relative to the nozzle flow direction, is independent of the projectile's pitch, namely,  $32^\circ$ , see Fig. 9. Also for positive pitch ( $+4^\circ$ ), the overpressure region upstream of the jet is more extended compared to  $0^\circ$ , and that for negative pitch angle ( $-4^\circ$ ) is less significant.

## 4 Numerical CFD cross flow/jet modeling

### 4.1 General remarks and governing equations

For predicting the flow around the jet-controlled projectile the CFX-TASCflow code (AEA Technology Engineering Software Ltd., Waterloo, Ontario, Canada), is applied for solving the conservation equations of mass, momentum and energy for the dependent variables: velocity, pressure and enthalpy. The calculations are carried out for a stationary, turbulent and compressible flow field (Gnemmi and Seiler, 2000). The standard turbulence model is implemented for modeling the turbulent flow behavior. For cross flow modeling the air species  $O_2$  and  $N_2$  are taken into account as well as the jet gas species  $CO$ ,  $CO_2$ ,  $H_2$ ,  $H_2O$ ,  $N_2$ .

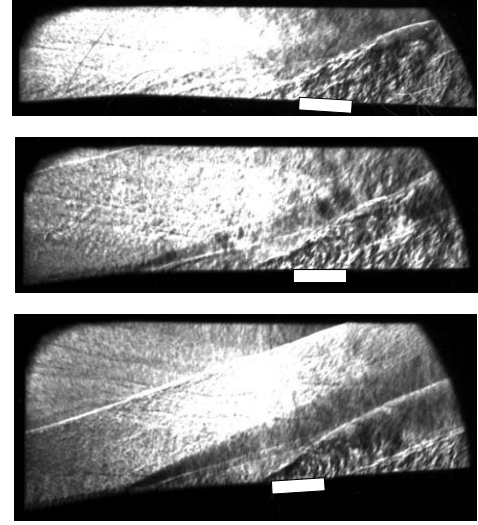


**Fig. 9.** Interferogram pictures with  $0^\circ$  jet angle, 1.5 km conditions

In turbulent flows, the dependent parameters are time-dependent. These quantities are assumed to be composed of a mean and a fluctuating value. The mean form of the equations is obtained through a time-averaging process, usually called Reynolds-stress averaging, and a technique of mass-averaging, also called Favre averaging (Cebeci and Smith 1974). The original equations for the conservation of mass, momentum and energy may be expressed in Cartesian tensor form (with the Einstein summation convention) in terms of time- and Favre- averaged quantities, respectively:

$$\frac{\partial \bar{\rho}}{\partial t} + \frac{\partial}{\partial x_j} (\bar{\rho} \tilde{u}_j) = 0 \quad (1)$$

$$\frac{\partial}{\partial t} (\bar{\rho} \tilde{u}_i) + \frac{\partial}{\partial x_j} (\bar{\rho} \tilde{u}_j \tilde{u}_i) = - \frac{\partial \bar{P}}{\partial x_i} - \frac{\partial}{\partial x_j} \left( \overline{\tau_{ij}} - \overline{\rho u_i'' u_j''} \right) + \overline{S_{ui}} \quad (2)$$

$$\begin{aligned} \frac{\partial}{\partial t} (\bar{\rho} \tilde{H}) - \frac{\partial \bar{P}}{\partial t} + \frac{\partial}{\partial x_j} (\bar{\rho} \tilde{u}_j \tilde{H}) &= - \frac{\partial}{\partial x_j} (\overline{q_j} + \overline{\rho u_j'' h''}) \\ &+ \frac{\partial}{\partial x_j} [\tilde{u}_i (\overline{\tau_{ij}} - \overline{\rho u_i'' u_j''}) + \overline{u_i'' \tau_{ij}''}] + \overline{S_E} \end{aligned} \quad (3)$$

In the above equations, a bar ( $\bar{\phantom{x}}$ ) represents the time-averaged component of a variable, a tilde ( $\tilde{\phantom{x}}$ ) indicates the Favre averaged component of a variable and the double prime ( $''$ ) indicates the fluctuating component arising from the mass-averaged process;  $t$  represents the time,  $\rho$  is the density,  $u_i$  represents the velocities in the  $x_i$ -coordinate directions,  $P$  is the static pressure,  $h$  the static enthalpy,  $H$  the total enthalpy,  $\tau_{ij}$  the viscous stress tensor,  $q_j$  the molecular energy transport due to heat conduction, and the  $S$  terms are additional source terms.

Equations (2) and (3) contain terms that cannot be expressed as a function of the mean flow variables:

the Reynolds stresses ( $\overline{\rho u_i'' u_j''}$ ), turbulent energy fluxes ( $\overline{\rho u_j'' h''}$ ) and the fluctuating viscous work term ( $\overline{u_i'' \tau_{ij}''}$ ). These terms are related to known quantities by using a turbulence model in order to close the equations. For the computations presented here, the well-known  $k - \varepsilon$  two-equation turbulence model is used to provide a link between the turbulent transport of momentum and energy and the mean flow variables and fluid properties. Since all the variables are mean flow quantities, it is customary to drop the symbols of time- and Favre-averaging. Finally, the mean conservation equations are as follows:

$$\frac{\partial \rho}{\partial t} + \frac{\partial}{\partial x_j}(\rho u_j) = 0 \quad (4)$$

$$\begin{aligned} \frac{\partial}{\partial t}(\rho u_i) + \frac{\partial}{\partial x_j}(\rho u_j u_i) = & -\frac{\partial P}{\partial x_i} \\ & + \frac{\partial}{\partial x_j} \left[ \mu_{\text{eff}} \left( \frac{\partial u_i}{\partial x_j} + \frac{\partial u_j}{\partial x_i} \right) - \frac{2}{3} \mu_{\text{eff}} \frac{\partial u_l}{\partial x_l} \delta_{ij} \right] + S_{ui} \end{aligned} \quad (5)$$

$$\begin{aligned} \frac{\partial}{\partial t}(\rho H) - \frac{\partial P}{\partial t} + \frac{\partial}{\partial x_j}(\rho u_j H) = & \frac{\partial}{\partial x_j} \left( \lambda \frac{\partial T}{\partial x_j} + \frac{\mu_t}{Pr_t} \frac{\partial h}{\partial x_j} \right) \\ & + \frac{\partial}{\partial x_j} \left\{ u_i \left[ \mu_{\text{eff}} \left( \frac{\partial u_i}{\partial x_j} + \frac{\partial u_j}{\partial x_i} \right) - \frac{2}{3} \mu_{\text{eff}} \frac{\partial u_l}{\partial x_l} \delta_{ij} \right] + \mu \frac{\partial k}{\partial x_j} \right\} + S_E \end{aligned} \quad (6)$$

in which  $\mu_{\text{eff}} = \mu_t + \mu$ . The eddy viscosity  $\mu_t$  is calculated from the product of a turbulence velocity scale ( $\approx \sqrt{k}$ ) and a turbulent length ( $\approx k^{3/2}/\varepsilon$ ) and yields:

$$\mu_t = \rho c_\mu \frac{k^2}{\varepsilon} \quad (7)$$

where  $\varepsilon$  is the dissipation rate of the turbulent kinetic energy  $k$  and  $c_\mu$  are model constants.  $\mu$  is the dynamic viscosity of the fluid.  $\delta_{ij}$  is the Kronecker symbol,  $\lambda$  represents the fluid heat conductivity and  $Pr_t$  the turbulent Prandtl number. Local values of  $k$  and  $\varepsilon$  are obtained from a solution of two semi-empirical transport equations (Launder and Spalding 1974).

CFX-TASCflow is a pressure-based code that was originally best suited for subsonic to low-speed compressible flows. The basic version of the code is unable to compute high-temperature air chemistry and consequently the code cannot be used to calculate the flow around a reentry vehicle, for example, which flies at very high supersonic Mach numbers in the Earth's atmosphere. A problem of pressure-based codes, such as CFX-TASCflow, is that the total pressure is not conserved even in the inviscid, shockless limit, since the algorithms are not locally based on gasdynamic laws.

However, a particular development of the code has been made to take into account the high Mach number compressible flow in order to calculate the flow field around projectiles and missiles with a very good accuracy. High-speed modeling and numerics improvements are implemented in the code to include:

- the velocity divergence or the second coefficient of viscosity contribution to the stresses and the correspond-

ing term of the compressible Reynolds stress model in the momentum balance (second term of the right hand side of Eq. (5));

- the viscous work term and the modeled Reynolds stress work term in the total energy equation (second term of the right hand side of Eq. (6));
- the compressible turbulent kinetic energy production model in the turbulent kinetic energy equation.

The standard  $k - \varepsilon$  turbulence model and its Kato-Launder extension used in the present computation employs a wall function to model the viscous near-wall layer. The wall function approach eliminates the necessity of numerically solving the large gradients in the thin near-wall region, thus keeping valuable computer resources.

Numerical simulations presented in this paper are performed for a projectile Mach number of 4.4, so moderate air temperatures develop behind the bow wave and deviations from real gas to perfect gas behavior are extremely small. Therefore, in this study, the accuracy of the code is not highly influenced by high Mach number effects.

The predictions of the flow structure and of the aerodynamic coefficients for compressible flows in the subsonic ( $M = 0.6$ ) up to the supersonic flow regime ( $M = 4$ ) are done with complete confidence, validated by comparisons with experimental data and based on extensive experience at ISL (Gnemmi et al. 1999). The code in high supersonic regime is also validated up to Mach 6 (Berner et al. 1998, 1999).

## 4.2 Multicomponent fluid

The code has the capability to model fluid mixtures with an arbitrary number of different species. Each inert gas species of the mixture can have its own set of physical properties. The code will calculate appropriate average values of the properties for each control volume in the flow domain. These average values will depend both on the component property values and on the proportion of each component present in the control volume.

The following assumptions have been made when implementing the multicomponent fluid model:

- it is assumed that the constituent components are miscible, that is, interfaces cannot be modeled;
- the model uses only a single field of velocity and temperature values;
- it is further assumed that the diffusion velocity of a component obeys Fick's law.

The bulk motion of the fluid is modeled using single velocity, pressure, temperature and turbulence fields. The influence of the multiple components is felt only through property variation taking into account the differing properties for the various components.

## 4.3 Grid specification

The symmetry axis of the jet exit is located at the center of gravity abscissa of the projectile due to the grid con-

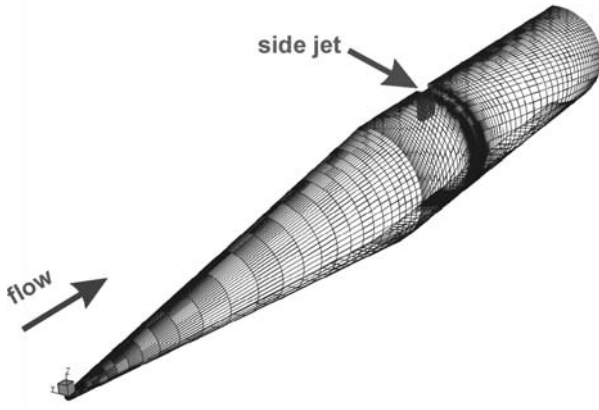


Fig. 10. Computational grid for the TZN projectile

struction. The computation domain is reduced to a cylindrical volume surrounding the projectile forebody and the wake is not computed. The prismatic jet grid is attached to the cylindrical part of the projectile. Different grids are used, depending on the Mach number of the cross-flow and on the jet flow. The upstream boundary surface of the larger grid is located one caliber ahead of the projectile nose. In the radial direction, the cylindrical boundary surface lies at six calibers from the rotational axis. A total of  $145 \times 45 \times 45$  nodes are distributed in the cross-flow domain for the finest grid. The prismatic jet domain is 21.5 mm long in the stream wise direction and 12.7 mm wide for all cases. The inlet boundary surface is located 20.7 mm inside the jet's channel for the gas jet simulations;  $31 \times 20 \times 40$  nodes are distributed for the biggest jet grid. Figure 10 depicts the computational grid of half the TZN projectile, the side jet mesh is indicated.

#### 4.4 Boundary conditions

The flow field is assumed to be compressible and turbulent. Having no information about the turbulent aspect of the flow, one specifies that the turbulent kinetic energy,  $k$ , and its dissipation rate,  $\epsilon$ , are constant along inlet regions, that is, the turbulent rate and the eddy length scale equal 1% and 7.5 mm respectively. The boundary conditions of the cross-flow are similar to those of the shock tube. The velocity vector, the static temperature and the static pressure are set at the nodes of inlet regions, whereas a supersonic outlet is used for the nodes of outlet regions.

The inlet boundary conditions of the jet flow are computed for an ideal gas by the 3D Reynolds averaged Navier-Stokes code FLOWer (Aumann et al. 1998) to simulate the jet flow alone in two dimensions (Meuer et al. 1999, Reisch and Meuer 1999). In addition for the hot jet, a computation of a one-dimensional expanding flow consisting of an ideal gas mixture in chemical equilibrium is necessary. The computation is carried out using the NASA rocket performance code, CET89 (McBride 1989), for approximating the exhaust composition obtained from the propellant supplier.

#### 4.5 Solver

The CFX-TASCflow code is a finite volume method that uses four discretization schemes: the upstream differencing scheme (UDS), the mass weighted scheme (MWS), the linear profile scheme (LPS) and a scheme (MLPS) which is intermediate between the last two. The first scheme is the most robust, whereas the linear profile scheme is the most accurate. A physical advection correction (PAC) may be activated for each discretization scheme to increase the accuracy of the computation.

A convergence criterion ends the computation and allows a stationary converged solution of the problem to be obtained. This criterion is defined as the maximum current dimensionless residual value for each equation (4) to (6). A computation is started from a constant initial flow field by using the most robust discretization scheme and a local time step. All computed solutions presented in this paper are converged up to  $10^{-3}$ . They are carried out by using the MLPS discretization and the PAC schemes in order to obtain a second-order solution.

### 5 Results and discussion

#### 5.1 Experimental work

Figure 11 shows a series of images for comparison with the numerical simulation. The interaction shock in front of the lateral jet is well established as is the mixing zone. The interaction shock angle is determined from image 6 as  $32^\circ$ . The bow shock formed at the projectile nose can be observed in the upper left-hand corner of the images. The corresponding chamber pressure and Pitot pressure were presented in Figs. 5 and 6, respectively.

#### 5.2 Numerical simulations

The ratio of the jet stagnation pressure to the cross-flow stagnation pressure,  $R_{Pt}$ , is defined in order to characterize the interaction of the side jet and the cross-flow of a projectile. It is convenient to quantify the efficiency of the lateral jet by defining a force amplification factor  $K_F$  and a pitching moment amplification factor  $K_M$  (Champigny and Lacau 1994). The former is defined as sum of the interaction force  $F_i$  and the jet thrust  $F_j$  normalized by the jet thrust:

$$K_F = \frac{F_i + F_j}{F_j}. \quad (8)$$

The interaction force  $F_i$  is calculated by integrating the computed pressures exerted on the projectile surface, the external flow and the side jet being turned on. The jet thrust  $F_j$  is determined by integrating the computed total pressures exactly over the jet exit, the external flow being turned off. The second amplification factor  $K_M$  is specially defined since the jet acts near the center of gravity of the projectile:

$$K_M = \frac{M_i + F_j D}{F_j D}. \quad (9)$$

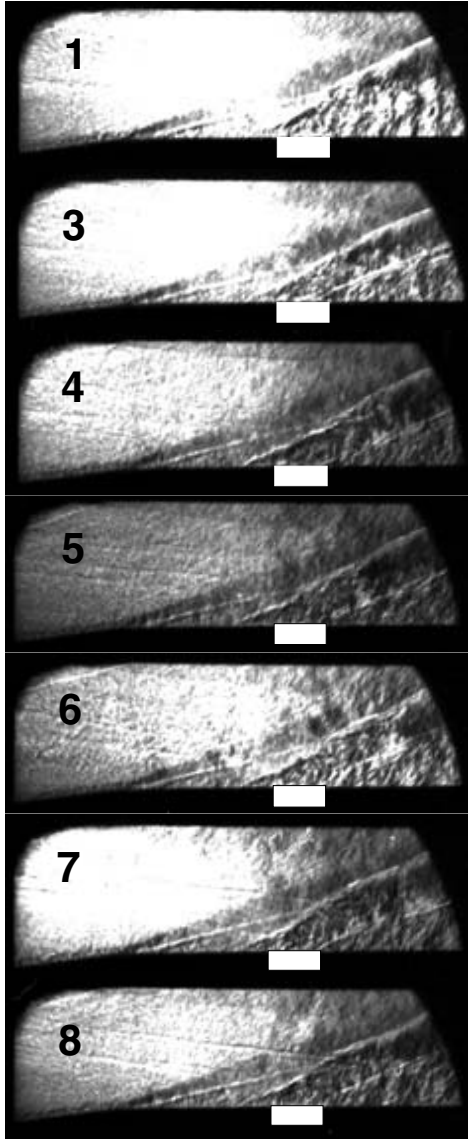


**Fig. 11.** Interferogram sequence with model at  $0^\circ$  pitch and  $0^\circ$  jet inclination

where  $M_i$  is the interaction pitching moment evaluated at the projectile center of gravity;  $D$  is the projectile diameter. An amplification factor greater than one indicates an increase of the total force or moment produced by the jet, while an amplification factor lower than one indicates a decrease of the total force or moment produced by the jet.

The evaluation of the interaction amplification factors necessitates three types of computation for each cross-flow Mach number.

- A computation of the jet flow without the cross-flow ( $Mf \approx 0$ ,  $Mj \neq 0$ ) for the jet thrust  $F_j$  determination.
- A computation of the cross-flow without the side jet ( $Mf \neq 0$ ,  $Mj = 0$ ). This computation is necessary in order to correct the third type of computation to take into account the non-uniformity of the projectile grid (Fig. 10). In fact, the computational grid is refined

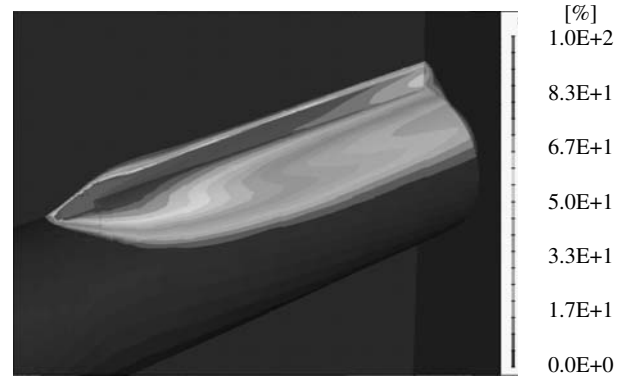


**Fig. 12.** Concentration of the gas mixture in the cross-flow,  $Mf = 4.5$ , 1–2 km of altitude

around the side jet whereas it is coarse on the lower side of the projectile.

- A final computation of the interaction of the lateral jet and the cross-flow ( $Mf \neq 0$ ,  $Mj \neq 0$ ) for the interaction force  $F_i$  and moment  $M_i$  calculation.

### 5.3 Hot jet results

The computations were carried out for a projectile flying between 1 and 4 km of altitude at Mach numbers of 3.5, 4 and 4.5. The static temperature of the cross-flow is 293 K and the static pressure is between 65 and 85 kPa. Previous two-dimensional computations carried out by TZN used a specific heats ratio of 1.21 and an average molecular weight of 25.35 kg/kmol for the combustion products. The mixture computed with the CET89 code is composed of 5 main gas components: 34% of CO, 18.5% of CO<sub>2</sub>, 18% of H<sub>2</sub>, 17% of H<sub>2</sub>O and 12.5% of N<sub>2</sub>. The transport properties (dynamic viscosity  $\mu$ , thermal conductivity  $\lambda$ , molecular diffusivity  $\Gamma$ ) of each gas are determined from handbook data. Analytical expressions are calculated following the law proposed by Oertel (1966):

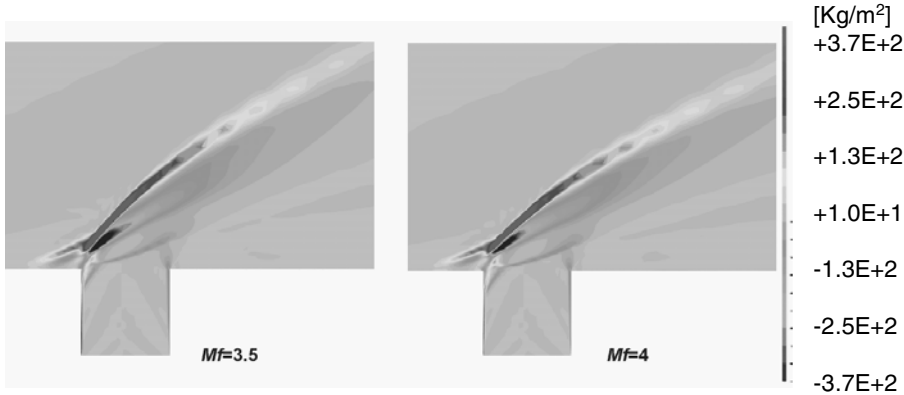
$$\frac{D_i}{D_n} = \left[ \frac{T_i}{T_n} \right]^\beta ; \quad (10)$$

where  $D$  represents either  $\mu$ ,  $\lambda$  or  $\Gamma$  variables. Variables with an  $n$  subscript are values at known conditions and values of the exponent  $\beta$  are given by Oertel (1966). The mixture composition allows analytical expressions for the gas mixture to be determined, so as to introduce transport properties into CFX-TASCflow.

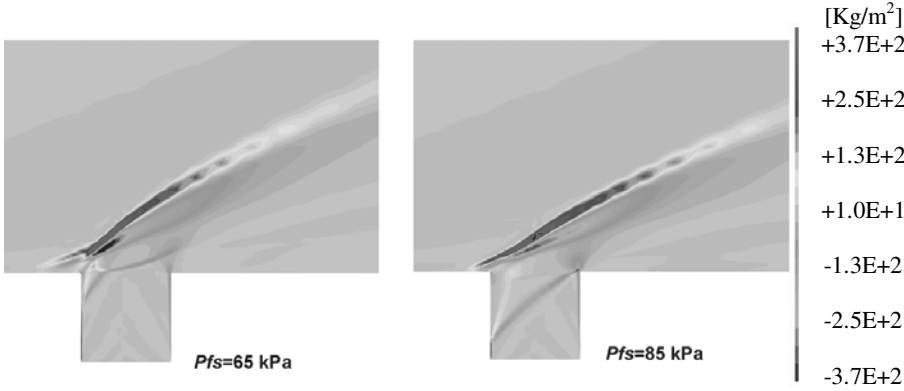
The mean quantities of the variables are used as jet inlet boundary conditions for the present three-dimensional computations. The jet mean static temperature and pressure are 1470 K and 61 kPa, respectively, and the jet mean velocity is 1700 m/s. These data lead to a stagnation pressures ratio  $R_{Pt}$  lower than 0.5. These jet inlet boundary conditions are set for the jet section located 20.7 mm inside the projectile jet channel.

Figure 12 shows the concentration of the gas mixture of the hot jet in the cross-flow. The mixing of the hot





**Fig. 13.** Density gradient distribution, hot jet, 3–4 km of altitude ( $P_{fs} = 65$  kPa)



**Fig. 14.** Density gradient distribution, hot jet,  $M_f = 4.5$

**Table 1.** Amplification factor vs. Mach number

$M_f$	$R_{Pt}$ ratio	$C_D$	$K_F$	$K_M$
3.5	0.43	0.0959	1.11	1.53
4.0	0.34	0.0903	1.21	1.49
4.5	0.27	0.0858	1.31	1.45

**Table 2.** Amplification factor vs. air pressure

$M_f$	$R_{Pt}$ ratio	$C_D$	$K_F$	$K_M$
65	0.27	0.0858	1.31	1.45
70	0.25	0.0853	1.29	1.48
75	0.24	0.0849	1.26	1.50
85	0.21	0.0841	1.22	1.57

jet with the external flow and the expansion of the jet plume are clearly visible. Figure 13 depicts the density gradient fields near the jet exit for  $M_f = 3.5$  and 4, the projectile flying between 3 and 4 km of altitude (65 kPa). Figure 14 presents the same kind of results for  $M_f = 4.5$ . The projectile is situated between 3 and 4 km of altitude on the left-hand side (65 kPa) whereas it flies between 1 and 2 km of altitude on the right-hand side (85 kPa). The separation shock angle formed by interference of cross and jet flow is deduced from the computations to be  $32^\circ$  and  $35^\circ$  for the 1.5 and 3.5 km altitude cases.

Table 1 summarizes the computed results for altitude conditions between 3 and 4 km, i.e.  $P_{fs} = 65$  kPa and for Mach numbers of 3.5, 4 and 4.5. With increasing Mach number, the force amplification factor increases from  $M = 3.5$  to  $M = 4.5$  by 18%. In contrast, the moment amplification factor and the drag coefficient drop slightly. In Table 2, the computed results at the cross-flow Mach number of 4.5 for different atmospheric pressures, corresponding to altitude conditions between 1 and 4 km,

are indicated. The drag coefficient decreases slightly at lower altitudes. The force amplification factor decreases by about 7% with altitude from 65 kPa to 85 kPa atmospheric pressure, whereas the moment amplification factor slightly increases. Increasing projectile speed enhances the side jet efficiency, whereas rising air pressure, i.e. lower altitudes, reduces its action.

#### 5.4 Comparison of results

Figure 15 depicts the computed pressure distributions on the projectile surface and in the jet exit. The beginning of the jet exit is located at  $x = 0$ . Upstream of the jet exit, the pressure increase due to the separation zone and due to the bow shock is well recognizable. Downstream, a low-pressure region is produced by the jet expansion. Figure 16 presents the same pressure distributions as in Fig. 15 but on a line that is located at 10.5 mm from the projectile symmetry plane, measured along the projectile surface.

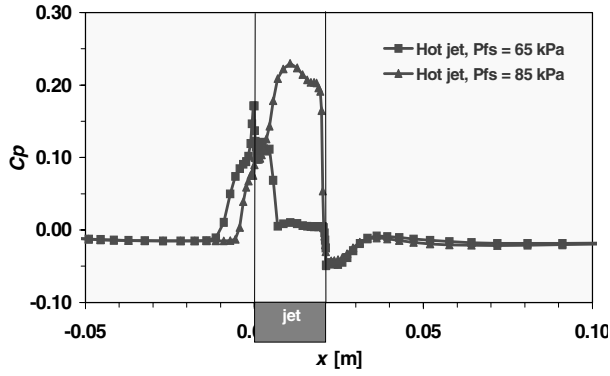


Fig. 15. Pressure distributions along the projectile symmetry plane,  $Mf = 4.5$

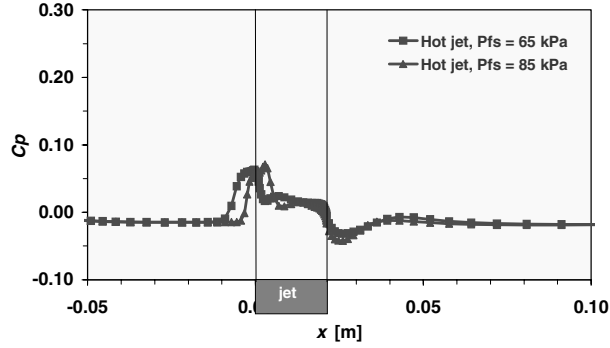


Fig. 16. Pressure distributions along a sideways line,  $Mf = 4.5$

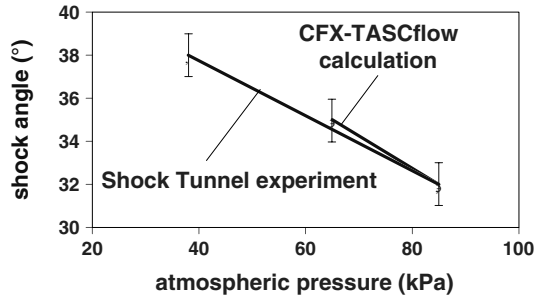


Fig. 17. Shock angle vs. air pressure (lines for visual aid only)

These figures show the three-dimensional aspect of the flow field formed by the jet/cross-flow interaction. The jet interaction angle dependence in the experiment versus air pressure, is depicted in Fig. 17 in comparison with those deduced from the computations. The agreement of both curves lies within the experimental error of  $\pm 1^\circ$ .

The jet shock angle behavior versus pitch angle depicted in Fig. 18 shows that the interaction shock orientation develops more steeply from negative to positive pitch angles. As previously discussed, it seems that at positive pitch the jet is more efficient with a larger overpressure region in front of the side jet than for negative pitch. For the jet axis oriented at  $0^\circ$  the interaction shock is much steeper than for the  $-30^\circ$  orientation, producing probably a more effective jet interference behavior.

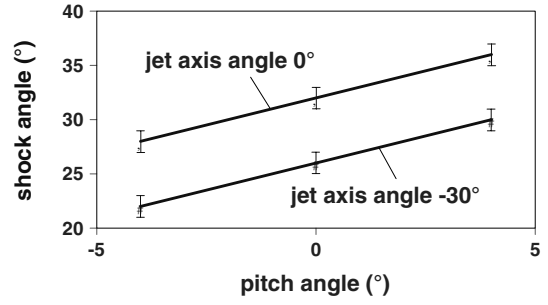


Fig. 18. Jet shock angle vs. pitch angle (lines for visual aid only)

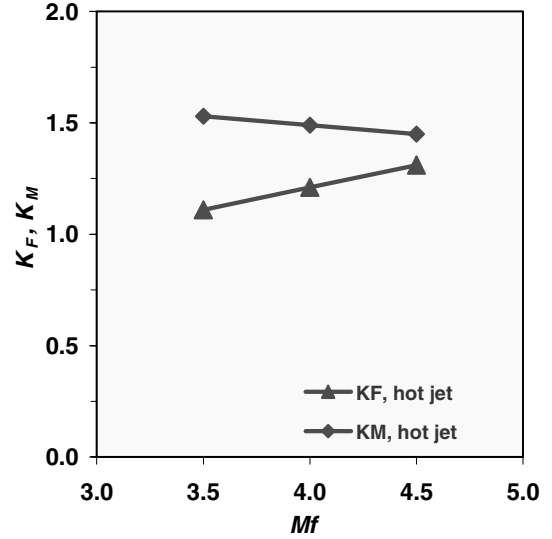


Fig. 19. Force amplification factor (lines for visual aid only)

The results concerning the calculated amplification factors are summarized in Fig. 19 versus Mach number. With increasing Mach number the force amplification increases. The moment in contrast drops.

## 6 Conclusions

The flow around a 90 mm caliber hypervelocity projectile, equipped with a side jet for producing lateral forces on the projectile's body to control its trajectory during flight, is investigated using a shock tunnel at a flight Mach number of 4.4, and at 1.5 and 7.5 km altitude conditions. The interaction of the lateral jet with the cross flow is visualized using differential interferometry at  $-4^\circ$ ,  $0^\circ$  and  $+4^\circ$  angle of attack. Numerical simulations for a stationary flow field around the jet-controlled projectile are carried out by means of the 3D CFX-TASCflow code.

The angles of the interaction shock in front of the lateral jet, deduced from computed results and the interferograms showed good agreement. The CFX-TASCflow code calculated the force and moment amplification factors  $K_f$  and  $K_M$  which are necessary for flight control applications. With  $K_f$  about 20–30% larger than one, the TZN projectile can successfully operate during its atmospheric

flight taking advantage of the provided full side jet engine thrust.

*Acknowledgements.* We would like to acknowledge the support of the German Ministry of Defense and of M. Schwenzer, N. Rosner and R. Meuer of Rheinmetall DETEC Unterlüss, Germany.

## References

- Aumann P, Bartelsheimer W, Bleecke, H, Eisfeld B, Leiser J, Heinrich R, Kroll N, Kunz M, Monsen E, Raddatz J, Reisch U, Roll N (1998) FLOWer Handbook. DLR Doc. Nr. Megaflow-1001
- Berner C, Fleck V, Warken D (1998) Aerodynamic Predictions of Optimized Explosively Formed Penetrators. 17th Int. Symp. & Exhibition on Ballistics, Midrand, South-Africa, 23–27 March 1998
- Berner C, Fleck V (1999) Pleat and Asymmetry Effects on the Aerodynamics of Explosively Formed Penetrators. 18th Int. Symp. & Exhibition on Ballistics, San Antonio/TX, USA, 15–18 Nov. 1999
- Cebeci T, Smith AMO (1974) Analysis of Turbulent Boundary Layers. Acad. Press, Inc., New-York, USA
- Champigny P, Lacau RG (1994) Lateral Jet Control for Tactical Missiles. AGARD R-804, Special Course on Missile Aerodynamics
- Gnemmi P (1999) Aérobalistique du projectile d'observation: Etude théorique de solutions d'intégration du dispositif optique dans la pointe. ISL Rep. R 121/99
- Gnemmi P, Sommer E, Naumann KW, Junod E (1999) Aerothermal Study of a Projectile in Flight: Experiment-Computation Comparison. 18th Int. Symp. & Exhibition on Ballistics, San Antonio/TX, USA, 15–18 Nov. 1999
- Gnemmi P, Seiler F (2000) Interaction of lateral jet with the projectile external flow. AIAA-paper 2000-4196
- Launder BE, Spalding DB (1974) The Numerical Computation of Turbulent Flows. Comp Meth Appl Mech Eng 3: 269–289
- McBride B (1989) CET89—Chemical Equilibrium with Transport Properties (Computer Program for Calculation of Complex Chemical Equilibrium Compositions, Rocket Performance, Incident and Reflected Shocks, and Chapman-Jouguet Detonations. NASA SP-273
- Meuer R, Rosner N, Schwenzer M (1999) The Development of Multiple Supersonic Hot Gas Actuators for Missile Control. RTA-Symp., Small Rocket Motors and Gas Generators for Land, Sea and Air Launched Weapon Systems, Corfu, Greece, 19–23 April 1999
- Naumann KW, Srujijes J (1985) Die Steuerung mittels seitlich austretender Strahlen. Literaturübersicht. ISL Rep. R 117/85 (in German and French)
- Oertel H (1966) Stoßrohre, Springer, New York
- Oertel H sen., Oertel H jr. (1989) Optische Strömungsmesstechnik, G. Braun Verlag, Karlsruhe
- Reisch U, Meuer R (1999) Numerical and Experimental Investigation of the Flow through a Fluidic Jet Reaction Control Element. DLR-FB
- Seiler F, Gnemmi P, Ende H, Havermann M, Schwenzer M (2001) Study on Lateral Jet/Cross Flow Interaction in the High Energy ISL Shock Tunnel. 23rd Int. Symp. on Shock Waves, Fort Worth, Texas, USA, July 22–27, 2001
- Zukoski EE, Spaid FW (1964) Secondary Injection of Gases into a Supersonic Flow. AIAA J 2(10): 1689–1696